ACS NANO

www.acsnano.org

ARTICLE

Photothermal Annealing-Enabled Millisecond Synthesis of Carbon Nanoonions and Simultaneous Single-Atom Functionalization

Dogyeong Jeon,[¶] Hamin Shin,[¶] Jun-Hwe Cha,[¶] HongHui Kim, Seohak Park, Jaewan Ahn, Su-Ho Cho, Chungseong Park, Dong-Ha Kim, Euichul Shin, Hionsuck Baik, Jihan Kim, Sung-Yool Choi,* and Il-Doo Kim*

Cite This: https://doi.org/10.1021/acsnano.5c11229

Read Online

ACCESS | Metrics & More | Article Recommendations | Supporting Information

ABSTRACT: **Carbon nanoonions (CNOs), known for their nanometer-scale surface curvature and potential for versatile functionalization, are widely used in energy and environmental applications. However, they face challenges from energy-intensive synthesis and time-consuming post-treatments, resulting in low yields and poor-quality sp^2 shells, which limit their commercial viability. In this study, we introduce a direct-contact annealing (DCA) platform reaching up to 3030 K within 1.4 ms (2.2×10^6 K s^{-1}), utilizing black-colored photothermal agents for millisecond-scale synthesis of CNO under ambient air. Moreover, we demonstrate simultaneous in situ single-atom catalyst (SACs) functionalization with eight different metal elements on the outer surface of CNOs. A case study on Pt SAC-functionalized CNOs demonstrates outstanding hydrogen evolution reaction performance. This DCA platform provides a promising alternative to conventional harsh conditions for SAC/CNO electrocatalyst synthesis, enabling ultrafast and facile production of surface-functionalized catalysts with exceptional energy efficiency and scalability advantages for advanced energy applications.**

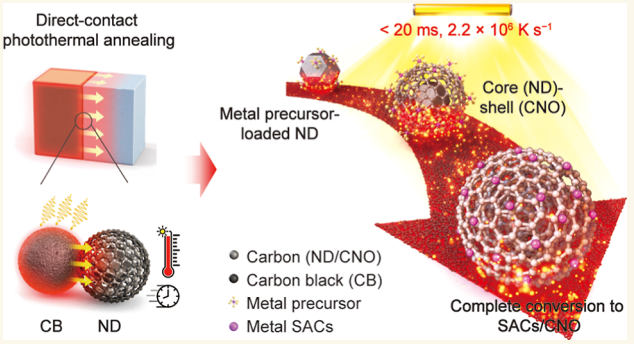

KEYWORDS: *carbon nanomaterials, single-atom sites, surface-functionalization, ultrarapid synthesis, hydrogen evolution reaction*

To meet the growing global energy demand and mitigate the environmental impact of a fossil fuel-dependent society, innovative, efficient, and sustainable solutions are essential.[1] Carbon, the second most abundant element in the biosphere after oxygen, forms diverse allotropes such as carbon nanotubes, fullerenes, graphite, and graphene, which are widely utilized as renewable energy and environmental nanomaterials. Carbon nanoonion (CNO), composed of concentric sp^2 spherical carbon shells, is one of the newest classes of carbon nanomaterials. Considering their high conductivity and chemical stability, CNO serves as electrodes or substrates in various electrochemical reactions.[2,3] Smaller CNOs (5−10 nm) exhibit higher reactivity than larger ones due to increased surface strain caused by their higher curvature. The surface chemistry of CNOs can be precisely tailored through functionalization with heteroatoms such as nitrogen and boron[4−6] and also single-site metal catalysts,[7−9] which make them versatile for applications in supercapacitors,[3,10,11] energy storage,[12] electrochemical sensors,[13,14] and electrocatalysis.[8,15]

The fabrication of CNOs involves removing surface functional groups from nanodiamonds (ND) to expose carbon atoms with dangling bonds. These bonds undergo reconstruction, forming sp^2-hybridized carbon shells starting from the ND outer layer and progressing inward to create multiple concentric layers. The broader utilization of CNOs faces significant challenges due to limitations in their conventional methods of synthesis. The widely used industrial technique entails annealing ND precursors at temperatures exceeding 1500 °C,[8,16,17] but the long annealing time (~20 h including ramping/cooling) and the requirement for high-vacuum systems present practical challenges. Recent advances in alternative methods, such as chemical vapor deposition,[18−20]

Received: July 4, 2025
Revised: September 11, 2025
Accepted: September 12, 2025

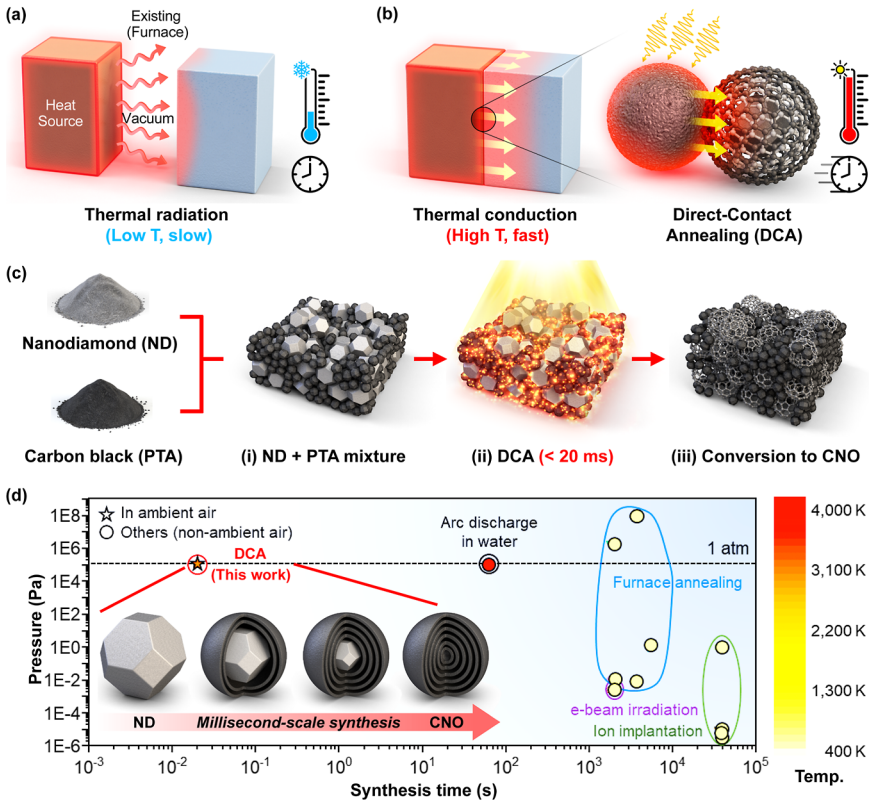

Figure 1. Introduction to the conceptual idea of PTA-assisted DCA. (a) Schematic illustration of existing high temperature annealing using the furnace and (b) DCA, this work. (c) Schematic illustration of DCA platform for CNO synthesis with PTAs. Homogeneous solution of ND, CB, and metal precursor is uniformly coated and dried on quartz slide glass. The slide glass is placed under a xenon lamp for IPL irradiation to activate the photothermal effect of CB. The temperature rapidly elevates up to 3030 K within 1.4 ms (2.2×10^6 K s^{-1}) and ND immediately transforms to CNO within 20 ms of pulsed light duration. (d) Time and vacuum pressure comparison of DCA against conventional advanced synthetic approaches for CNO fabrication and schematic representation of CNO transformation processes at the millisecond scale in DCA. The exact values for the time and pressure are listed in Table S1. The others displayed in circles include various types of nonambient air synthesis environments such as vacuum, reducing atmosphere, and solutions. The color in the Figure 1d indicates synthesis temperature from the colormap on the right. Illustration by B. J. Kim and used with permission from the artist.

arc discharge,[21,22] pyrolysis,[23,24] and laser irradiation,[25,26] have aimed to address these challenges. However, these methods still suffer from high power consumption, poor yield, and quality of CNOs, such that distorted oval shapes are created rather than a spherical form. In the most conventional pyrolysis for CNO synthesis, heat sources (e.g., inductor coils) and target materials are not in direct contact, leading to significant energy dissipation during the overall system temperature elevation. In that sense, the photothermal effect is a crucial manifestation of the energy conversion, wherein light energy is absorbed by a material and then re-emitted as thermal energy, contingent on the material's properties.[27] This effect is well-demonstrated in photothermal therapy, where photothermal agents (PTAs) generate heat upon exposure to light and are placed in direct contact with wounded areas for precise cell stimulation.[28,29] Expanding upon the localized direct-contact heating approach, we propose a pioneering use of the photothermal effect to convert ND into CNO by uniformly mixing PTAs and ND and subjecting them to photothermal annealing, facilitated by intense pulsed light (IPL) irradiation from a xenon flash lamp.[30−32]

Here, we developed a direct-contact annealing (DCA) platform by introducing black-colored PTAs, specifically carbon black (CB), to provide "heating spots" directly adjacent to the ND, thereby significantly raising the efficiency of thermal energy transfer. Our PTA-assisted DCA platform enables extremely fast, uniform, and large-area heat treatment in all CB-distributed regions. Molecular dynamics (MD) simulations revealed that the conversion from ND to CNO only requires several hundred picoseconds at 2600 K, given that rapid elevation to a sufficient temperature level is achieved. Utilizing this annealing platform, we demonstrate the complete conversion from ND to CNOs within the millisecond scale under ambient air conditions, thus eliminating the need for vacuum systems. The CB PTAs in our DCA platform rapidly raise the surrounding temperature up to 3030 K within 1.4 ms (2.2×10^6 K s^{-1}), resulting in more than 1000-fold improvement in energy consumption efficiency. Furthermore, we investigate the capability of the DCA platform for simultaneous in situ stabilization of universal single-atom catalyst (SACs) (SACs) onto CNOs. This serves as a demonstrational case study showcasing the ultrafast (<20 ms) alteration of the surface chemical properties of CNOs. Among various SACs (Pt, Ir, Ru, Cr, Cu, Co, Fe, and Ni), Pt SACs (Pt_1/CNO) exhibit outstanding catalytic performances in the hydrogen evolution reaction (HER) with an overpotential of 13.9 mV at 10 mA cm^{-2}, which is 3.47 times smaller than that of Pt SACs-stabilized CB (Pt_1/CB), demonstrating nearly optimal HER performance compared to that of reported atomic Pt species on carbon supports. Pt_1/CNO exhibits a mass activity of 2.0 A mg^{-1}_{Pt} at 13.9 mV, surpassing that of commercial Pt/C catalysts by 5.88 times.

https://doi.org/10.1021/acsnano.5c11229
ACS Nano XXXX, XXX, XXX−XXX

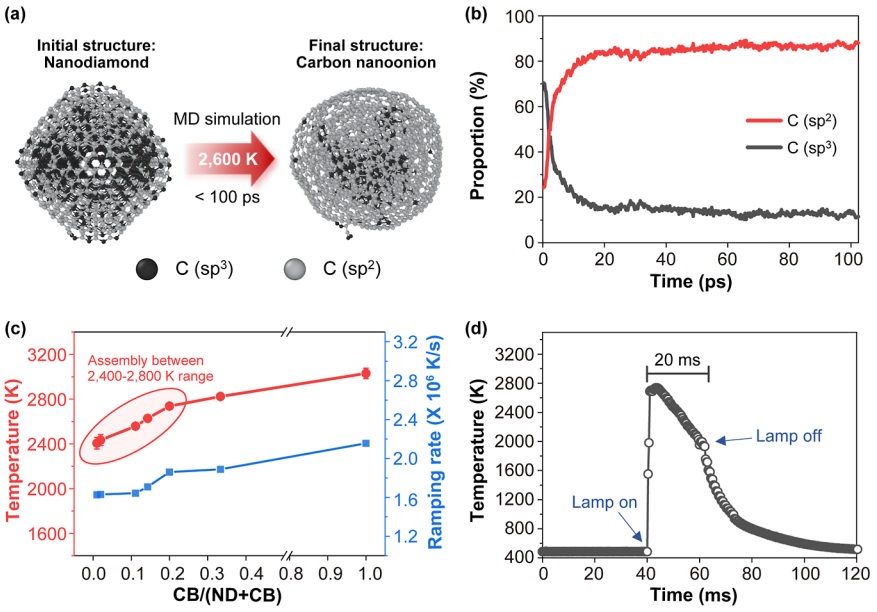

Figure 2. Temperature evolution with the increasing CB ratio and MD simulation for ultrarapid ND conversion to CNO. (a) Computationally simulated nanodiamond, and the resultant CNO after exposure to 2600 K for 100 ps. (b) Relative proportions of sp^3 and sp^2 hybridized carbon during the 102.4 ps (including heating-up time frame) of 2600 K heat treatment simulation. (c) Evolution of maximum surface temperature and temperature elevation rate for IPL irradiation on samples with the increasing CB concentration. (d) Dynamic temperature variation data of a 4:1 ratio sample under IPL irradiation acquired with an infrared (IR) camera.

The superior HER activity of Pt_1/CNO catalysts represents a significant advancement toward developing cost-effective and scalable hydrogen generation technologies that are essential for the clean energy transition. This work establishes a robust conceptual and experimental framework for advancing the controlled synthesis of carbon-based nanomaterials, specifically surface-functionalized CNO nanocatalysts embedded with single-atom active sites. By leveraging the DCA platform, this approach demonstrates a viable and efficient synthetic route that operates under ambient conditions and achieves reaction time scales previously inaccessible through conventional methodologies, thereby advancing scalable production of energy conversion materials.

RESULTS AND DISCUSSION

Direct-Contact Annealing Process. Conventional high-temperature annealing of carbon nanomaterials involves placing samples in a furnace surrounded by Joule-heated inductor coils within a vacuum chamber to prevent carbon decomposition. While this method is widely utilized and straightforward, thermal radiation primarily occurs in the absence or scarcity of fluid. As a result, the process tends to be time-consuming due to inefficient energy conversion from photon-based thermal generation with longer wavelengths (>1 μm) via blackbody radiation at temperatures below 2000 K (Figure 1a). In contrast, direct contact between heat sources and target materials facilitates thermal conduction through the interaction of vibrating atoms (phonon−phonon coupling) at the interface, minimizing the energy loss during conversion. Notably, the benefits of the direct-contact-based photothermal effect are demonstrated in photothermal therapy, a promising therapeutic approach. It involves injecting biocompatible PTAs into affected cells, where, upon exposure to external laser irradiation, activated PTAs generate heat that destroys nearby abnormal cells. The concept of DCA draws inspiration from the principles of localized heating applied in photothermal therapy, considering a new platform where controlled concentration of PTAs is evenly distributed and is in direct contact with target materials (Figure 1b). Introducing xenon lamps, which offer a larger beam area (>cm^2-scale) compared to lasers, enables the photothermal heating of the entire area encompassing the PTAs to temperatures exceeding 2000 K. Furthermore, our new platform facilitates time-saving processes by utilizing direct energy exchange from phonon to phonon, thereby achieving efficient energy conversion.

For the DCA process (Figure 1c), a mixture of nanodiamond (ND) powder (<10 nm particle size), homogeneously dispersed CB PTA, and metal precursors is prepared on transparent quartz slide glass (Figure S1). When the mixture is exposed to millisecond (ms)-scale high energy light produced by a xenon lamp under ambient conditions, the uniformly distributed CB converts the light energy into heat energy as PTAs, providing sufficient heat energy to the adjacent ND to transform into carbon nano-onions (CNO). Simultaneously, this step stabilizes metal ions as atomically isolated single-atom sites, which will be further elaborated on later in the following sections. Note that double-sided photothermal annealing was employed to minimize the temperature gradient between the top and bottom layers. In Figure 1d, we compare our DCA system with reported CNO synthesis methods, showing the superiority in terms of the synthesis time and the absence of the need for vacuum systems. The most rapid synthesis of <5 nm-sized CNO reported by Sano et al. requires 60 s in water,[21,22] whereas our work represents a grand advancement, achieving complete conversion to CNO within 20 ms under air ambient conditions.

The PTA-assisted DCA approach operates within an extremely narrow time window. Thus, validating the feasibility of a successful transition from sp^3 ND to high-quality sp^2 CNO within such a short time scale (20 ms) is crucial. Figure 2a illustrates the MD simulation result before and after applying

https://doi.org/10.1021/acsnano.5c11229
ACS Nano XXXX, XXX, XXX−XXX

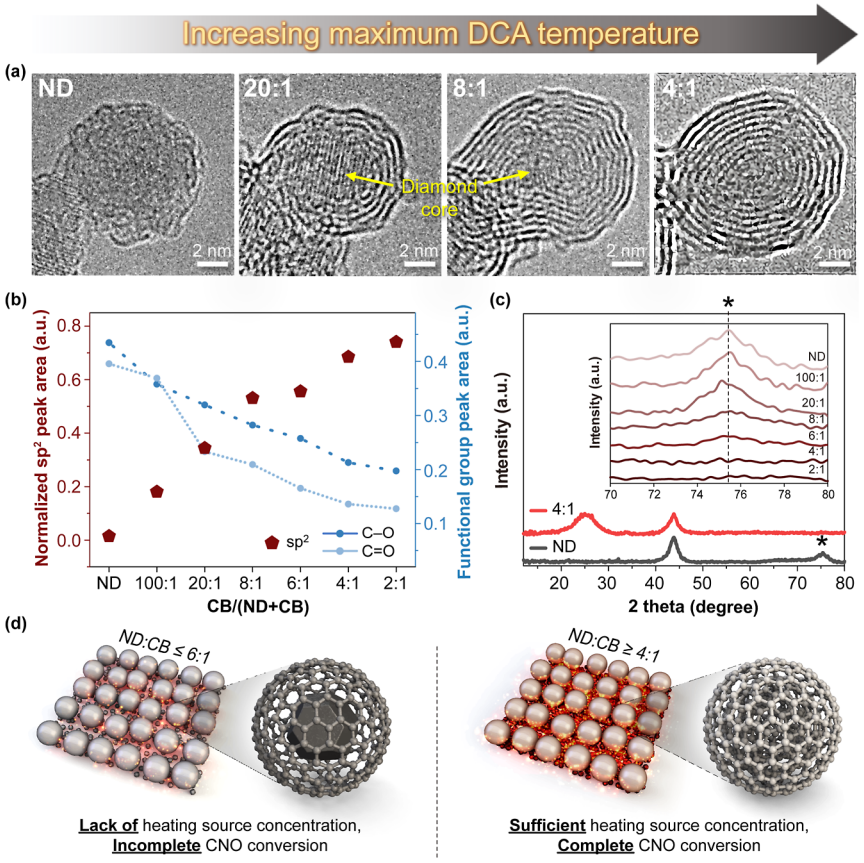

Figure 3. Structural and phase evolution of CNOs with increasing CB concentration in DCA. (a) Evolution of CNO morphology (quality) with increasing maximum DCA temperature observed with TEM. (b) Normalized sp^2 peak area and functional group peak areas of samples with different ND/CB ratios after IPL irradiation, determined from X-ray photoelectron spectroscopy (XPS) results. (c) X-ray diffraction (XRD) patterns of the 4:1 ND/CB sample and pristine ND. Inset is the XRD patterns of different ND/CB samples after IPL irradiation, magnified at the XRD 2θ between 70° and 80°. The (220) peak at 75.5° slightly remains for 8:1 and 6:1 samples as well, indicating incomplete transformation from ND to CNO, and the complete transformation occurs at a 4:1 ratio, where the peak finally vanishes. (d) Schematic illustration of the heating source (CB) concentration effect during the DCA process.

2600 K to a diamond nanoparticle model (Video S1). The theoretical study suggests that the estimated completion time for ND to CNO transition is < 100 ps (ps) (Figure 2b), which is a time scale five orders of magnitude shorter than the light pulse for the DCA process. While the transition from ND to CNO can occur rapidly, conventional methods often require a significant amount of excess energy and time to reach the high temperatures necessary to initiate the reaction. A more advanced simulation incorporating the—OH functional group, which is the most prevalent among the surface-terminating functional groups of ND (−OH, −OOH, and═O), reveals a slightly extended transition time (<300 ps) (Video S2 and Figure S2). The MD simulation thus demonstrates that the DCA process is indeed a highly viable approach for synthesizing CNOs on a millisecond scale. It highlights that the conversion from ND to CNO does not necessitate conventional time- and energy-consuming annealing processes as long as rapid temperature elevation is achieved.

The maximum surface temperature of the ND and CB mixture upon 20 ms of IPL irradiation is determined by controlling the mass ratio between ND and CB (Figures 2c and S3). The temperature exhibits marginal elevation with increasing CB content. (See Methods and Supplementary Notes for more details on the IR temperature measurement system). The trend of temperature ramping rate with increasing CB content aligns with the trend observed for maximum surface temperature, indicating that higher CB concentration at the surface facilitates rapid annealing. Using CB PTAs, the maximum surface temperature reached was measured at 3030 K, with a ramping rate of 2.2×10^6 K s^{-1}. Despite a marginal decline in its temperature upon the integration of ND, this is the fastest reported ramping speed, surpassing not only conventional CNO synthesis methods but also recent advanced rapid heating systems like microwave synthesis and arc discharge annealing.[21,22,24] After the lamp is turned off, the temperature immediately starts to decrease from the peak to the baseline (473 K) for 60 ms, achieving a cooling rate of 2.58×10^4 K s^{-1} (Figure 2d).

The evolution of the CNO phase and crystallinity after the DCA process, with increasing CB PTAs content, is analyzed using high-resolution transmission electron microscopy (Figure 3a) (for convenience, the samples are named by their relative mass ratio between ND and CB, i.e., ND/CB). Photothermal effects of ND, with a large optical band gap of 5.47 eV,[21] are mainly caused by midgap states that originate from defects and surface functional groups; however, this moderate electron excitation by photons is unlikely to exhibit a significant photothermal effect.[33,34] In this regard, the ND particles remained unchanged after IPL irradiation. With

https://doi.org/10.1021/acsnano.5c11229
ACS Nano XXXX, XXX, XXX−XXX

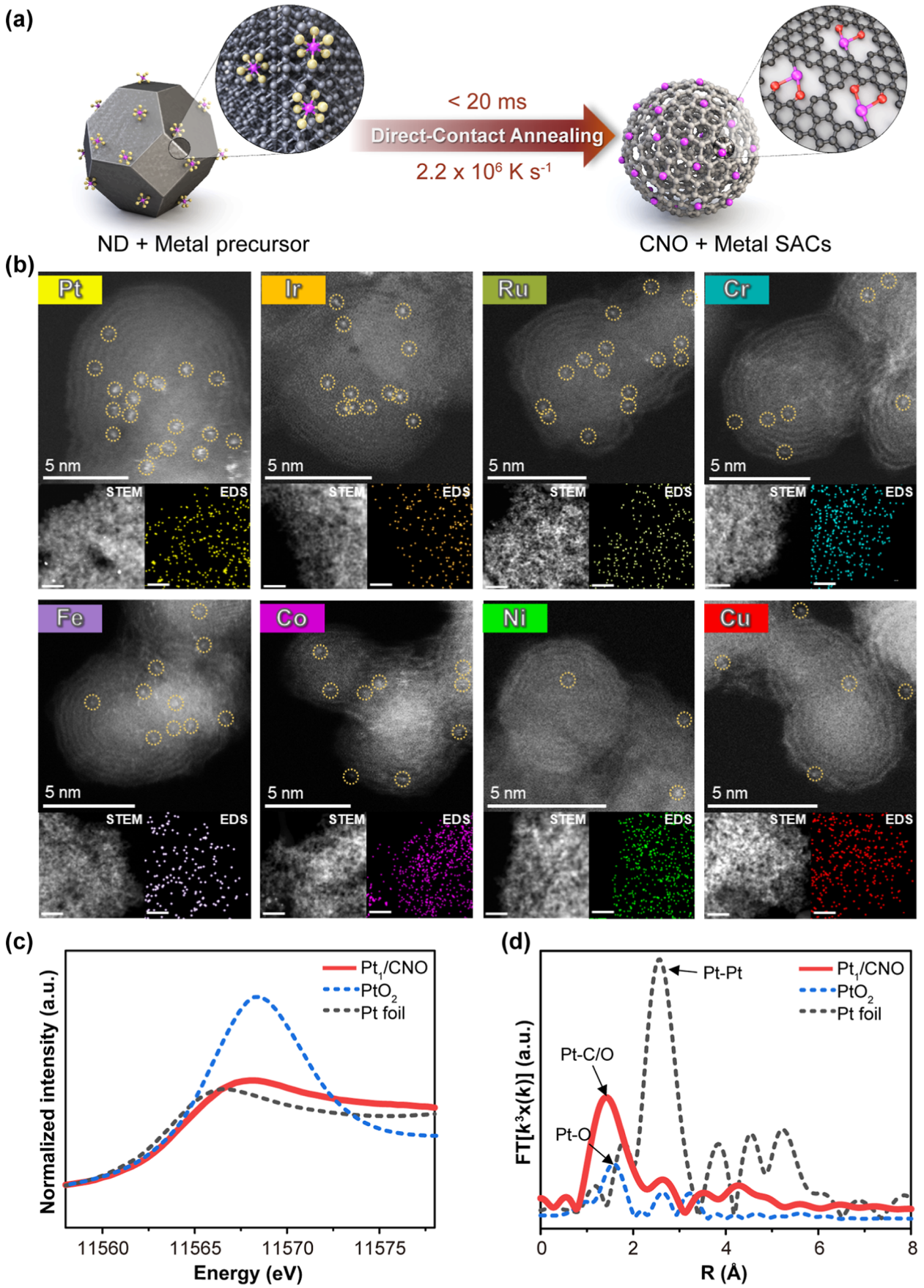

Figure 4. Characterization of SACs of various elements stabilized on the CNO surface. (a) Schematic illustration of simultaneous ND to CNO phase transition and SAC stabilization process using DCA. (b) STEM images of eight metal elements SACs stabilized on CNO and corresponding energy-dispersive X-ray spectroscopy (EDS) mapping images (scale of inset image: 50 nm). (c) X-ray absorption near-edge

https://doi.org/10.1021/acsnano.5c11229
ACS Nano XXXX, XXX, XXX−XXX

Figure 4. continued

spectroscopy (XANES) spectra of Pt_1/CNO and reference samples. (d) Extended X-ray absorption fine structure (EXAFS) spectra of Pt_1/CNO and reference samples.

increasing maximum DCA temperature, the transformation from sp^3 ND to spherical graphitic carbon structure begins to occur from the outer shell. At an ND(4):CB(1) ratio, full conversion to multilayer sp^2 shell-structured CNO is achieved.

In the analysis of C 1s XPS, the transformation from ND to CNO becomes evident with increasing CB PTAs content (Figure 3b). The increase in the normalized peak area of sp^2 carbon, along with the decrease in peak areas of major functional groups (Figure S4, Table S1), indicates the formation of higher quality CNO. Notably, increasing CB content has only a minor influence on the total area of sp^2 carbon (Figure S5). XRD patterns of the varied ratio samples corroborate the XPS data, where the ND (220) peak at 75.5° (Figure 3c, marked with an asterisk) shows a decreasing trend with increasing CB ratio after IPL irradiation (inset of Figure 3c). The complete transformation to CNO occurs at a 4:1 ratio, where the peak finally disappears. Furthermore, CB particles generally exhibit diameters in the range of 50−60 nm, whereas the CNOs synthesized from NDs in our study are significantly smaller, with diameters ranging from 5 to 10 nm. This size disparity unequivocally confirms that a portion of the synthesized CNOs is derived from NDs rather than from CB, as indicated by their markedly smaller dimensions (Figure S6). Moreover, we discovered that the thickness of the ND and CB mixture on the slide glass before IPL irradiation is a crucial factor. Ensuring optimal sample thickness is essential to facilitate efficient heat conduction from the surface to the core of the coated sample (see Figures S7 and S8).[35]

The maximum surface temperatures for various ND/CB ratios (Figure 2c), excluding pristine ND and CB, show a narrow distribution between 2400 and ~2800 K. Despite minor differences in surface temperatures, noticeable variations in the degrees of CNO transformation are observed with changes in CB content in the mixture. These differences can be attributed to the concentration of distributed CB in the samples during IPL irradiation. In other words, the increasing concentration of PTA "heating spots" in the mixture underscores the degree of direct-contact-based thermal conduction (Figure 3d). Therefore, utilizing the DCA platform emphasizes the importance of customizing the loading concentration of PTA among target materials. This involves considering not only the photothermal efficiency and the power of the IPL lamp but also the significance of the total area of shared interfaces between heat producers and absorbents.

We compared our findings with those of CNOs synthesized using only ND as the precursor, using the most typical method of furnace annealing. Raman spectroscopy, XRD, and TEM (Figure S9, with detailed caption) were used to examine the difference in the defects of DCA-fabricated CNO and furnace-fabricated CNO, and we found that there is no noticeable difference in the concentration of surface defects in the products of the two different synthetic approaches. Furthermore, to compare the surface chemical properties, particularly the oxygen content, an XPS 1s analysis was conducted (Figure S10, with a detailed caption). However, DCA-fabricated 4:1 CNO exhibits slightly higher electrical conductivity of 170.7 S/m than furnace-fabricated CNO (139.5 S/m), which can be attributed to whether the sample contains IPL-treated CB or not (Table S2). Beyond the photothermal effect that is the key to the DCA process, CB also has a high electrical conductivity of 231.6 S/m and 371.2 S/m before and after IPL treatment, respectively. The ability of the DCA platform to achieve rapid and efficient phase transformation in ambient air conditions represents a significant advancement in CNO synthesis techniques. By optimizing annealing time and leveraging the photothermal effect, it demonstrates a unique capability to produce high-quality CNOs within an extremely short time frame. Table S3 compares power consumption between the conventional furnace annealing under an inert atmosphere (12 kWh) and the DCA (0.011 kWh) for the synthesis of CNO. For the synthesis of 1 g of CNO, the power consumption is estimated to be approximately 55 times lower by introducing the DCA process.

DCA for Simultaneous In Situ Stabilization of Universal Single-Atom Catalysts. Besides the DCA for CNO synthesis, we demonstrate that the DCA system can be further exploited as an effective tool for simultaneous surface catalyst functionalization of the as-synthesized nanomaterials. Rapid thermal annealing techniques, similar to our DCA method, have been widely employed for the synthesis of nanoparticles and even SACs on the surface of carbon support materials.[36−42] It is widely known that a short burst of high temperatures can thermally degrade metal coordination complex ions into atoms, which can anchor them onto the defective carbon surface. Therefore, by simply incorporating metal precursor ions into the ND and CB mixtures prior to DCA, we hypothesized that the synthesis of CNO and the surface functionalization of metal SACs could be simultaneously achieved. Here, we present the DCA as a universal strategy for stabilizing various SACs on CNO, concurrently with the transformation from ND to CNO (Figure 4a).

Precursors of diverse metal elements, Pt, Ir, Ru, Cr, Cu, Co, Fe, and Ni, were adsorbed onto the surface of ND particles during sample preparation via solution-mediated impregnation prior to the DCA process (see Methods). The subsequent IPL irradiation, which causes the CNO transition, simultaneously removes ligands from the metal precursors and drives the formation of strong coordination bonds between the single-site metal ions and the outermost graphitic shell of CNO, forming SAC-stabilized CNO (M_1/CNO, where M is the metal element). MD simulation with metal atoms on each facet of ND (Video S3) reveals that the metal atoms remain well attached to the surface of the CNO after transformation. Furthermore, the metal atoms, originally positioned on the surface of ND, are slightly embedded at the same planar level as the outermost shell of CNO. TEM images further demonstrate that the interlayer distance of the onion-like graphitic shell in Pt_1/CNO is approximately 0.357 nm, which is consistent with that of CNO without Pt, supporting the claim that Pt single atoms are not trapped within the graphitic shell (Figure S11).

Aberration-corrected high-angle annular dark-field scanning transmission electron microscopy (HAADF-STEM) was used to resolve the SACs on CNO surfaces, where the atomic-site metal species were identified with localized bright spots generated by the large Z-contrast between metals and carbon

https://doi.org/10.1021/acsnano.5c11229
ACS Nano XXXX, XXX, XXX−XXX

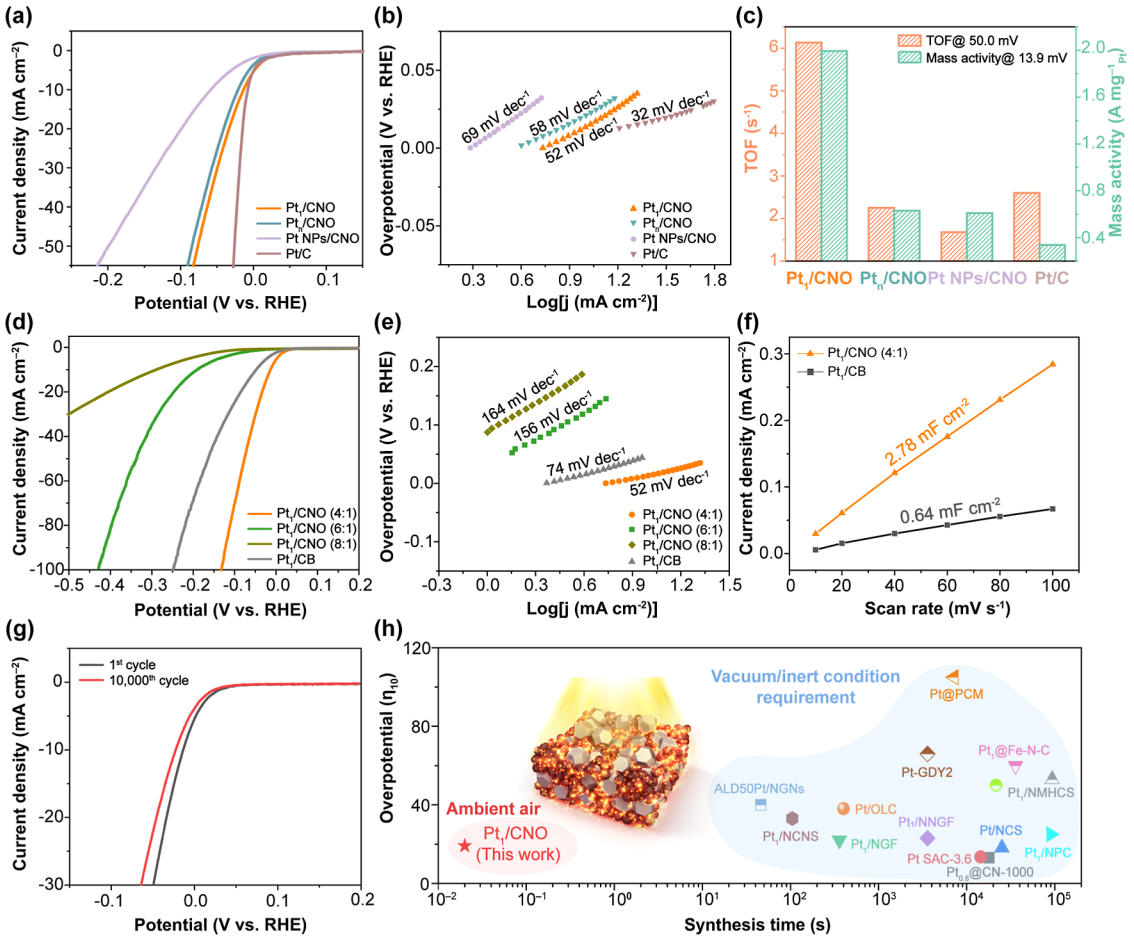

Figure 5. Electrocatalytic HER performances of Pt_1/CNO. (a) Polarization curves of Pt_1/CNO, Pt_n/CNO, Pt NPs/CNO, and Pt/C. (b) Tafel plots originated from LSV curves. (c) Calculated TOF and mass activity of Pt_1/CNO compared to the reference catalysts at 50.0 mV and 13.9 mV, respectively. (d) Polarization curves of Pt_1/CNO with different CB ratios. (e) Corresponding Tafel plots. (f) Double-layer capacitances (C_{dl}) of Pt_1/CNO and Pt_1/CB. (g) Polarization curves of Pt_1/CNO before and after 10,000 cyclic voltammetry (CV) cycles. (h) Comparison of the HER overpotentials regarding synthetic process time with the state-of-the-art catalysts in 0.5 M H_2SO_4. Exact values of the overpotentials and synthesis conditions for each material are listed in Table S7.

(Figure 4b). The HAADF-STEM images reveal well-dispersed single-atom metallic sites of all metal elements on CNO. This finding is further confirmed by EDS mapping results and EDS spectra (Figure S12). The loading amount of SACs on CNO, determined by inductively coupled plasma−mass spectrometry (ICP−MS), was found to be 0.12 at % (1.89 wt %) for Pt. Other metal SACs were similarly stabilized on CNO with comparable at. % loadings (Table S4).

We conducted XANES analysis to determine the electronic structures of the atomic-site metal catalysts on CNO. Pt SACs were selected as representatives for the various SAC metal elements. Figure 4c shows the Pt L_3-edge XANES spectra of Pt_1/CNO. The dominant features of Pt_1/CNO are located between the photon energies of metallic Pt (Pt foil, Pt^0) and Pt oxide (PtO_2, Pt^{4+}), indicating the cationic environment of the Pt SACs. This observation is further supported by deconvoluted Pt 4f XPS spectra of Pt_1/CNO (Figure S13).

The cationic nature of SACs is commonly attributed to the formation of coordination bonds between the single metal atoms and the support material. The coordination environment of the SACs on CNO was investigated using EXAFS measurement on eight M_1/CNO samples, with a particular focus on Pt_1/CNO and reference samples (Figure 4d). A single major peak appeared at 1.5 Å in the EXAFS spectra of Pt_1/CNO, corresponding to Pt−C/O bonds, which are slightly shorter to the Pt−O bonds of PtO_2. The spectral features of Pt_1/CNO are markedly distinct from those of the metallic Pt reference (Pt foil), with no visible Pt−Pt contribution, indicating the absence of Pt clusters and nanoparticles. We performed data fitting on the EXAFS spectra of eight M_1/CNO samples (Figure S14, Table S5) and determined that the average coordination number for the M-C_1 contribution is 1.28 ± 0.17, while the coordination number for the M-O contribution is 2.1 ± 0.28. This indicates that the atomically dispersed metal species are stabilized on CNO by one C atom and two O atoms (Figure 4a), in the same planar level as that of the graphitic shell, consistent with the observations from the MD simulation (Video S3). The EXAFS results verify that the metal species of all eight elements are atomically stabilized on the surface of CNO. More specifically, under the optimized low-loading conditions used in this work, the formation of atomically dispersed metal sites on CNO is favored over nanoparticle growth. The millisecond-scale heating−cooling profile of the DCA process (Figure 2d) limits the time available for long-range surface diffusion and nucleation, while the graphitic shells of CNO provide coordination sites that stabilize individual metal atoms during the flash. Consistent with this anchoring motif, MD simulations reveal that atoms

https://doi.org/10.1021/acsnano.5c11229
ACS Nano XXXX, XXX, XXX−XXX

placed on the ND surface remain attached after conversion and become slightly embedded within the same planar level as the outermost CNO shell. However, when precursor loading is deliberately increased beyond this range, nanoparticles can form, as observed in Pt nanocluster-stabilized CNO (Pt_n/CNO, Figure S15) controls, confirming that aggregation is kinetically and thermodynamically suppressed under our standard synthesis conditions. This finding confirms the universal capability of the DCA process for functionalizing CNO with SACs.

DCA for Hydrogen Evolution Reaction Catalysts. SACs achieve not only the highest level of atom efficiency among metal catalysts, but also unprecedented catalytic properties that are substantially distinct from those of their higher nuclearity counterparts due to the higher oxidation state and altered coordination environments.[43−48] In particular, SACs stabilized on carbon supports with nanometer-scale surface curvature have recently been discovered to exhibit superior catalytic activities over those of two-dimensional (2D) planar carbon supports, as well as the commercial Pt/C.[8] Inspired by the earlier works, recent research employed the density functional theory calculations to screen single transition metal atoms supported on CNO as a promising avenue for developing highly efficient HER catalysts.[7] The catalytic enhancement effect resulting from utilizing SACs and curved CNO supports was validated by evaluating the electrocatalytic performance for the HER using the rotating disk electrode technique in N_2-saturated 1 M $HClO_4$ electrolyte. For comparison, Pt_1/CNO, Pt nanoclusters-stabilized CNO (Pt_n/CNO, Figure S15), Pt NPs-stabilized CNO (Pt NPs/CNO, Figure S16), and commercial Pt/C are prepared by the same DCA process. As shown in the linear sweep voltammetry (LSV) plots in Figure 5a, it is worth noting that the overpotential of Pt_1/CNO (13.9 mV at 10 mA cm^{-2}) is significantly lower than Pt_n/CNO (21.1 mV at 10 mA cm^{-2}), indicating that the utilization of Pt SACs (1.87 wt %) in HER is more effective than Pt nanoclusters (4.37 wt %). However, Pt_n/CNO contains both Pt SACs and nanoclusters, and to enable a more precise comparison of the HER catalytic activity between single atoms and nanoclusters or nanoparticles, we stabilized Pt NPs approximately 3 nm in size onto CNO, ensuring that the total Pt loading was identical to that in the single-atom form in Pt_1/CNO, further highlighting the catalytic performance of SACs. The HER LSV results show that Pt NPs/CNO, which contains only particles, exhibits a higher overpotential (58.7 mV at 10 mA cm^{-2}) compared to Pt_1/CNO. These findings confirm the superior HER performance of single atoms rather than NPs. Additionally, the Tafel slopes of Pt_1/CNO, Pt_n/CNO, Pt NPs/CNO, and Pt/C were 52 mV dec^{-1}, 58 mV dec^{-1}, 69 mV dec^{-1}, and 32 mV dec^{-1}, respectively (Figure 5b), reflecting that Pt_1/CNO shows higher HER kinetic activity compared to Pt_n/CNO and Pt NPs/CNO. The turnover frequency (TOF) is a measure of an electrocatalyst's intrinsic activity, defined as the number of H_2 molecules generated per active site per unit of time. Figure 5c presents a comparison of TOF and mass activity of all samples normalized to the Pt loading at the same overpotential of 50.0 and 13.9 mV, respectively. Assuming that all Pt atoms are electrocatalytically active, the TOF values of the Pt_1/CNO approach as high as 6.13 s^{-1}, outperforming not only Pt_n/CNO (2.25 s^{-1}), Pt NPs/CNO (1.68 s^{-1}) but also Pt/C (2.60 s^{-1}). Pt_1/CNO indeed demonstrates superior mass activity of 2.0 A mg^{-1}_{Pt}, which is 3.17, 3.27, and 5.88 times higher than those of Pt_n/CNO (0.63 A mg^{-1}_{Pt}), Pt NPs/CNO (0.61 A mg^{-1}_{Pt}), or Pt/C (0.34 A mg^{-1}_{Pt}), respectively. Furthermore, with SACs synthesized with eight different metal elements on CNO supports (M_1/CNO), we evaluated their HER performance (Figure S17). The loading of diverse metal elements demonstrated that the CNO support is highly adaptable, capable of stabilizing various single metal atoms while maintaining structural integrity and catalytic accessibility, thereby underscoring its broad applicability across different SAC systems.

To highlight the advantages of CNO, we compared the HER performance of Pt SACs with different ratios of ND to CB (Pt_1/CNO (4:1), Pt_1/CNO (6:1), and Pt_1/CNO (8:1)) and Pt SACs-stabilized CB (Pt_1/CB, pure CB without CNO, Figure S18). As previously described, increasing the CB PTAs ratio leads to a higher maximum temperature during DCA treatment, which induces a gradual transformation from sp^3-hybridized ND to spherical graphitic carbon, beginning from the outer shell. At a 4:1 ND to CB ratio, this transformation reaches completion, resulting in a multilayer sp^2 shell-structured CNO. As shown in the LSV curves, Pt_1/CNO (4:1) exhibits the highest HER activity, requiring a significantly lower overpotential to reach 10 mA cm^{-2} compared to those of Pt_1/CNO (6:1) (190 mV at 10 mA cm^{-2}) and Pt_1/CNO (8:1) (290 mV at 10 mA cm^{-2}) (Figure 5d). This superior performance is attributed to the enhanced nanocurvature effects of the fully developed multilayer sp^2 carbon shell structure of the CNO. To get further insight into the nanocurvature effect of CNOs, we compared the HER performance of Pt_1/CNO (4:1) with that of Pt_1/CB. As a result, Pt_1/CNO (4:1) exhibits a noticeably higher HER activity compared to Pt_1/CB (48.2 mV at 10 mA cm^{-2}), implying that protons can be more readily distributed around atomically dispersed Pt on CNO due to the unique single-atomic curved supports of CNO.[8] The Tafel slopes of Pt_1/CNO (4:1), Pt_1/CNO (6:1), Pt_1/CNO (8:1), and Pt_1/CB were 52 mV dec^{-1}, 156 mV dec^{-1}, 164 mV dec^{-1}, and 74 mV dec^{-1}, respectively, indicating Pt_1/CNO (4:1) has a faster hydrogen production reaction rate (Figure 5e). Additionally, electrochemical double-layer capacitance (C_{dl}) measurements were also applied to estimate the electrochemical active surface area (ECSA) (Figures 5f and S19). The C_{dl} value of Pt_1/CNO (2.78 mF cm^{-2}) was larger than that of Pt_1/CB (0.64 mF cm^{-2}), suggesting that it shows a larger ECSA, which is proportional to the C_{dl}. This is particularly due to the favorable nanocurvature with higher HER catalytic enhancement effect for Pt atoms immobilized on CNO. To evaluate the intrinsic activity of the catalysts, the LSV curves were normalized by ECSA, as detailed in Figure S20. Electrochemical impedance spectroscopy (EIS) measurements were performed to gain further insight into the HER kinetics at an overpotential of 50.0 mV (Figure S21). Pt_1/CNO exhibits a smaller value of charge transfer resistance (R_{ct}) compared to Pt_1/CB. To further demonstrate the long-term durability of Pt_1/CNO, we conducted accelerated degradation tests (Figure 5g). LSV curves of Pt_1/CNO show only a slight deterioration even after 10,000 cycles. Chronoamperometric curves demonstrate that Pt_1/CNO exhibited a slight decrease after more than 5 h of operation under 50.0 mV (Figure S22). Overall, the excellent electrochemical properties demonstrated by Pt_1/CNO can be attributed to the full utilization of single-site metallic catalysts and the distinctive structure of curved CNO supports. To further underscore the significance of this advancement,

https://doi.org/10.1021/acsnano.5c11229
ACS Nano XXXX, XXX, XXX−XXX

particularly in achieving high-performance HER catalysis within an ultrafast synthesis time (within 20 ms) via DCA, we compared the overpotential of Pt_1/CNO at 10 mA cm^{-2} with those of other recently reported atomic Pt species supported on carbon supports for HER electrocatalysts in 0.5 M H_2SO_4 (Figure 5h). The HER kinetics on Pt-based catalysts are known to be insensitive to the acid anion (e.g., ClO_4^- vs SO_4^{2-}),[49] a finding consistent with our control experiments (Figure S23). However, to enable a direct and fair comparison with contemporary works, the Pt_1/CNO catalyst was evaluated in 0.5 M H_2SO_4. Our DCA-based synthetic platform not only enables the ultrarapid formation of the unique structural and catalytic features of CNO, but also allows for the simultaneous in situ functionalization with a broad range of SACs, thereby providing a competitive and scalable route for fabricating efficient HER electrocatalysts.

CONCLUSIONS

We present a highly energy-efficient DCA strategy that exploits CB PTAs to transform nanodiamond precursors into CNOs within milliseconds while simultaneously anchoring SACs on their surface under ambient conditions. This unified synthesis-functionalization approach delivers 1000-fold improvement in energy consumption efficiency through rapid heating, eliminating vacuum system requirements, and energy-intensive prolonged processing that constrain scalable electrocatalyst synthesis. Pt_1/CNO catalysts exemplify this breakthrough with exceptional hydrogen evolution performance, achieving an overpotential of only 13.9 mV at 10 mA^{-2}. Notably, it is applicable not only to continuous carbon substrates but also to carbon particulates (Figure S24), offering a versatile and scalable platform for fabricating functional catalyst−support nanostructures without postsynthetic purification requirements. Overall, the DCA platform paves the way for a next-generation strategy for the efficient and versatile synthesis of nanoscale electrocatalysts, addressing the conventional trade-offs between synthesis time, energy consumption, and catalytic performance in advanced energy conversion applications.

METHODS

Pristine nanodiamond (ND) powder (nanopowder, <10 nm particle size (TEM), ≥97% trace metals basis), dimethylformamide (DMF), chloroplatinic acid hexahydrate ($H_2PtCl_6·6H_2O$), hydrogen hexachloroiridate hydrate ($H_2IrCl_6·xH_2O$), ruthenium(III) chloride hydrate ($RuCl_3·xH_2O$), chromium(III) nitrate nonahydrate ($Cr(NO_3)_3·9H_2O$), copper(II) chloride ($CuCl_2$), cobalt(II) chloride ($CoCl_2$), ferric (III) chloride ($FeCl_3$),, nickel(II) chloride hexahydrate ($NiCl_2·6H_2O$), and commercial Pt/C catalyst (20 wt % loading) were purchased from Sigma-Aldrich (St. Louis, USA). CB, Super P Conductive, 99+% (metals basis) was purchased from Alfa Aesar. All materials were used as received.

Synthesis of M_1/CNO by DCA. A ND and CB mixture (ND: 30 mg, CB: 7.5 mg) was dispersed in metal precursor-containing (2 mM of $H_2PtCl_6·6H_2O$, $H_2IrCl_6·xH_2O$, $RuCl_3·xH_2O$, $Cr(NO_3)_3·9H_2O$, $CuCl_2$, $CoCl_2$, $FeCl_3$, or $NiCl_2·6H_2O$) DMF solution (total volume of 2.4 mL), followed by 30 min of ultrasonication. The obtained dispersion was drop-coated on a glass substrate several times and dried on a hot plate at 60 °C until complete evaporation of DMF. After a homogeneous mixing and drop-coating process, IPL with a xenon flash lamp (PLT, Photocura) was utilized to achieve the DCA process for CNO synthesis (Figure S25). The flash light with broad-spectrum wavelengths from 300 to 1000 nm was generated by the xenon lamp. The intensity of the generated light can be controlled by sample distance from the lamp, pulse number, pulse on/off time, charged capacitance in capacitors, and adjusting the applied voltage. The glass substrate was placed on the moving-stage 2 cm away from the lamp. To maintain the output light energy as ∼40 J cm^{-2}, light irradiation condition was cautiously introduced with a pulse on-time of 20 ms and a constant voltage of 500 V. The light irradiation was alternately performed on both sides of the glass substrate. After the IPL irradiation, the samples were thoroughly washed with DMF and ethanol to remove excess metal precursors and impurities and then dried at 40 °C for 12 h in a vacuum.

Preparation of Pt_n/CNO and Pt_1/CB also followed the exact same procedure, except for Pt_n/CNO, 20 mM H_2PtCl_6-containing DMF solution was used, and for Pt_1/CB, 37.5 mg of pure CB was used without using the ND precursor.

We fixed the total mass of the mixture to 37.5 mg and varied the ratio between ND and CB, to obtain different ND/CB ratio samples (n:1, n = 2, 4, 6, 8, 20, 50, and 100) without the single-metal atom catalysts and followed same experimental procedure as M_1/CNO.

CB was not removed after the DCA process as the remaining CB can serve to increase the conductivity of the catalyst, and Pt_1/CB can further boost the HER performance.

Synthesis of CNO by Furnace Annealing. The furnace annealing was performed under typical conditions at 1500 °C[50,51] in an Ar atmosphere with a heating rate of 10 °C min^{-1} for 1 h, as this temperature is above the threshold (1200 °C) at which the CNO shell begins to form.[52]

IR Temperature Measurement System During IPL. In order to measure the momentary rise in surface temperature during the 20 ms flash light irradiation, two IR thermometers (1500 °C-sensor and 3000 °C-sensor) were used as IR sensors. For the 1500 °C-sensor (CTlaser 3MH2, Optris), the temperature range from 200 °C up to 1500 °C was accurately measured by detecting an IR element featuring a wavelength of 2.3 μm coming from samples. Note that the baseline of temperature was depicted at 200 °C since it was the lowest temperature that the 1500 °C-sensor is capable of detecting. However, the high photothermal efficiency of CB enabled heating above the upper limit (1500 °C) of the 1500 °C-sensor, thereby demanding a broadening of the measured temperature range. Accordingly, the other IR thermometer (3000 °C-sensor) was utilized for temperature measurement higher than 1500 °C. Besides the 1500 °C-sensor, the 3000 °C-sensor (thermoMETER CTRM-2H1SF100-C3, Micro-Epsilon) is capable of supporting temperature measurement up to 3000 °C by detecting IR information in the wavelength of 1.5 μm from the target during the 20 ms flash irradiation. Since the flashlight features broad-spectrum wavelengths including the IR region, we checked an IR noise effect generated from the Xe lamp to achieve accurate measurement and confirmed insignificant noise coming from the flashlight (Figure S26). The surface temperatures were measured with the emissivity value set at unity, which is a blackbody emissivity. Considering the real emissivity of the ND and CB mixture, an emissivity correction was applied for the accurate measurement (Figure S27). It should be noted that the emissivity correction renders the temperature upper limit of each IR sensor much higher than 1500 °C for the 1500 °C-sensor and 3000 °C for the 3000 °C-sensor, respectively. To guarantee the shortest time resolution of 1 ms according to the product specifications, a data acquisition system was set to correct and convert measured analog signals into digital signals (Figure S28). It is worth noting that that the change in temperature was observed with a time frame scale of 1 ms due to the limit of the time resolution in milliseconds; therefore, the actual temperature ramping rates could be higher than the values (∼10^6 K s^{-1}) reported in this study.

Structural Characterization. XRD measurements (D/MAX-2500, Rigaku) were performed using a high-resolution powder X-ray diffractometer with Cu Kα radiation. XPS (Sigma Probe, Thermo VG Scientific) was carried out using Al Kα radiation. TEM and EDS characterizations were carried out using a FEI Titan Themi-3 Double CS & Mono TEM equipped with the Chemi-STEM technology using a Super-X detector with XFEG (Korea Basic Science Institute, Seoul, Korea). Raman spectroscopy (ARAMIS, Horiba Jobin Yvon, Montpellier, France) with a 514 nm laser source was used to investigate the dominant vibration modes. The amount of metal

https://doi.org/10.1021/acsnano.5c11229
ACS Nano XXXX, XXX, XXX−XXX

component compared to carbon was measured with Agilent ICP−MS. XAS measurements were performed on beamline 10C at the Pohang Accelerator Laboratory (PAL, Pohang, South Korea). All XAS spectra were acquired at room temperature in fluorescence mode using a double-crystal Si(111) monochromator. Analyses of both the near edge (in energy scale) and extended range (in R space) XAS spectra were performed using Athena software, and fitting was performed using Artemis software.

Simulations. The initial structure of the nanodiamond (ND) was obtained from the Materials Project database,[53] where a diamond unit cell was used to generate a supercell with an 8 × 8 × 8 dimension, modified to have a truncated octahedron shape. The truncated octahedron structure has been previously found to be stable in other studies and closely resembles the Wulff crystal of carbon.[54,55] The final ND cluster consisted of 2048 carbon atoms with a diameter of 2.8 nm. In addition to the pristine ND cluster, we also constructed a hydroxyl-functionalized ND cluster by attaching hydroxyl groups on the (111) facets (a total of 8 planes in the cluster) of the pristine cluster. To simulate the movement of a Pt atom during phase transformation, we also constructed a system with 8 Pt atoms on the surface of the pristine ND cluster. The cluster was placed in the center of a cubic unit cell with a 100 Å lattice constant.

We used Reactive Force Field (ReaxFF) to describe the interactions of atoms, and LAMMPS codes to conduct the MD simulation.[56,57] The ReaxFF developed by Chenoweth et al. was used for the pristine ND and hydroxyl-functionalized ND,[58] while the Pt atom added system was simulated by using the ReaxFF developed by Sanz-Navarro et al.[59] We performed the simulation in a canonical ensemble (NVT, constant volume and constant temperature ensemble) using the Nosé−Hoover thermostat with a time step of 0.2 fs. All systems underwent a five-step simulation process: energy minimization (using the steepest gradient method), 10 to 300 K heat up for 10^4 time-steps (i.e., 2 ps), 300 K NVT for 10^5 time-steps (i.e., 20 ps), 300 K to 2600 K heat up for 10^4 time-steps (i.e., 2 ps), and 2600 K NVT for 5×10^5 time-steps (i.e., 100 ps). In the case of the hydroxyl-functionalized ND, an additional NVT simulation at 2600 K for 5×10^5 time-steps (i.e., 200 ps in total) was conducted to reach the convergence of the system.

To evaluate the formation of bonds, we analyzed the number of sp^3 and sp^2 carbon atoms with a cutoff distance of 1.8 Å. Carbon atoms that form bonds with three other carbon atoms are considered sp^3 carbons, while those with bonds with two atoms are considered sp^2 carbons. We used Ovito visualizer for the simulation visualization.[60]

Electrochemical Measurements. Electrochemical measurements were performed in a three-electrode electrochemical setup using a Wonatech Zive MP1 multichannel potentiostat. The glassy carbon working electrode was polished with alumina powder (0.3 and 0.05 μm diameters) from Pine. Then, 4 mg of each catalyst with 80 μL of 5 wt % Nafion solution (Sigma-Aldrich) was dispersed in 1 mL of a water/isopropanol mixed solvent (1:3 volume ratio) by 1 h of sonication to get a uniform suspension. After vigorous mixing with ultrasonication, 14 μL of the catalyst ink was deposited on the glassy carbon disk, which resulted in a catalyst loading of 265 μg cm^{-2}. A graphite rod and a Ag/AgCl-saturated KCl electrode served as the counter and reference electrode, respectively. Prior to data collection, the electrolyte was saturated under a given N_2 atmosphere for 5 min, then calibration was carried out using a CV with a sweep rate of 20 mV s^{-1}. LSV was performed with a potential range from −0.1 to 1.1 V vs Ag/AgCl, which was conducted in 1 M $HClO_4$ solution at a scan rate of 50 mV s^{-1}. The potentials were calculated after *iR* correction by $E_{iR\text{-corrected}} = E$ (vs reversible hydrogen electrode (RHE)) − *iR*, where *i* is the current, and *R* is the uncompensated solution resistance (without *iR* correction shown in Figure S30).

The ECSA of the electrode was estimated by the C_{dl} according to the following equation

$$\mathrm{ECSA} = \frac{C_{dl}}{C_s}$$

where C_s is the specific capacitance of the sample, or the capacitance of a flat surface, generally found to be in the range of 20−60 μF $^{-2}$.

The TOF was calculated using the following equation, assuming that all of the Pt sites were active.

$$\mathrm{TOF} = \frac{\text{total hydrogen turnovers per geometric area}}{\text{active sites per geometric area}}$$

$$\mathrm{TOF} = \frac{j}{2\mathrm{F} \times \mathrm{n}}$$

where *j* is the current density (A cm^{-2}) at a specific overpotential, the number 2 indicating a two-electron HER, *F* is Faraday's constant (96485.3C mol^{-1}), and n represents the moles of Pt on the working electrode.

EIS measurements were carried out at an overpotential of 50.0 mV with a 5 mV AC potential from 0.1 to 1×10^6 Hz. An accelerating degradation test was evaluated using 10,000 continuous cycles between −0.05 and 0.2 V (vs RHE). All potentials were converted to RHE using the equation *E* (vs RHE) = *E* (vs Ag/AgCl) + 0.197V + 0.059pH V, where 0.197 V was obtained by calibrating the Ag/AgCl electrode against the RHE in 1 M $HClO_4$.

ASSOCIATED CONTENT

Data Availability Statement

The authors declare that the data supporting the findings of this study are available in the paper, Supporting Information. Additional data sets related to this study are available from the corresponding author on reasonable request.

Supporting Information

The Supporting Information is available free of charge at https://pubs.acs.org/doi/10.1021/acsnano.5c11229.

Photographic image of ND/CB-coated quartz slide glass; CB concentration dependence on DCA temperature; graphic MD result for −OH-decorated ND under 2700 K; XPS analysis on samples with different ND/CB ratios after IPL irradiation, XPS peak area comparison for sp^2 carbon before and after DCA treatment, and TEM image of CNO and annealed CB; cross-sectional SEM of samples with different coating numbers and XRD results of samples with different coating numbers after IPL irradiation; characterization between furnace-CNO and 4:1 CNO and XPS detailed scans of the O region of furnace-CNO and IPL-CNO; TEM images of CNO and Pt_1/CNO, EDS spectra of M_1/CNO, XPS analysis on Pt_1/CNO in Pt4*f*, EXAFS data and fitting results of M_1/CNO, HAADF-STEM image of Pt_n/CNO and Pt NPs/CNO; electrocatalytic HER performances of M_1/CNO; HAADF-STEM image of Pt_1/CB, the double-layer capacitance measurements at different scan rate, ECSA-normalized current density and mass activity for Pt_1/CNO and Pt_1/CB, Nyquist plots of the catalysts, chronoamperometry curves of Pt_1/CNO, and HER performance of Pt_1/CNO in 1 M $HClO_4$ vs 0.5 M H_2SO_4; comparison between DCA and CTS; IPL system overview, xenon lamp performance overview, ND/CB ratio and emissivity, IPL measurement system interface, and temperature−time graph measured using 1500 °C and 3000 °C sensors; LSV curves of Pt_1/CNO before and after *iR*-correction; XPS peak area calculation from Figure S5; conductivities for various samples using 4-point probe method; comparison of power consumptions; ICP results for all metal elements of M_1/CNO sample and EXAFS fitting table for all M_1/CNO samples; comparisons of synthetic methods for carbon

https://doi.org/10.1021/acsnano.5c11229
ACS Nano XXXX, XXX, XXX−XXX

nano-onions and comparisons of overpotentials and synthetic condition of state-of-the-art HER catalysts; and emissivity of different ND/CB ratio samples (PDF)

MD simulation with a pure ND nanoparticle under 2600 K (MP4)

MD simulation with −OH surface terminating group ND nanoparticles under 2600 K(MP4)

MD simulation with eight Pt atoms-anchored ND nanoparticles under 2600 K (MP4)

AUTHOR INFORMATION

Corresponding Authors

Sung-Yool Choi − *School of Electrical Engineering, Graduate School of Semiconductor Technology, KAIST, Daejeon 34141, Republic of Korea;* orcid.org/0000-0002-0960-7146; Email: sungyool.choi@kaist.ac.kr

Il-Doo Kim − *Department of Materials Science and Engineering, Korea Advanced Institute of Science and Technology (KAIST), Daejeon 34141, Republic of Korea;* orcid.org/0000-0002-9970-2218; Email: idkim@kaist.ac.kr

Authors

Dogyeong Jeon − *Department of Materials Science and Engineering, Korea Advanced Institute of Science and Technology (KAIST), Daejeon 34141, Republic of Korea*

Hamin Shin − *Department of Materials Science and Engineering, Korea Advanced Institute of Science and Technology (KAIST), Daejeon 34141, Republic of Korea; Human-centered Sensing Laboratory, Department of Mechanical and Process Engineering, ETH Zurich, Zurich CH-8092, Switzerland;* orcid.org/0000-0001-8330-5448

Jun-Hwe Cha − *School of Electrical Engineering, Graduate School of Semiconductor Technology, KAIST, Daejeon 34141, Republic of Korea*

HongHui Kim − *Department of Chemical and Biomolecular Engineering, KAIST, Daejeon 34141, Republic of Korea;* orcid.org/0000-0002-1527-8641

Seohak Park − *School of Electrical Engineering, Graduate School of Semiconductor Technology, KAIST, Daejeon 34141, Republic of Korea*

Jaewan Ahn − *Department of Materials Science and Engineering, Korea Advanced Institute of Science and Technology (KAIST), Daejeon 34141, Republic of Korea;* orcid.org/0000-0002-0136-8427

Su-Ho Cho − *Department of Materials Science and Engineering, Korea Advanced Institute of Science and Technology (KAIST), Daejeon 34141, Republic of Korea*

Chungseong Park − *Department of Materials Science and Engineering, Korea Advanced Institute of Science and Technology (KAIST), Daejeon 34141, Republic of Korea*

Dong-Ha Kim − *Department of Materials Science and Engineering, Korea Advanced Institute of Science and Technology (KAIST), Daejeon 34141, Republic of Korea; Department of Materials Science and Chemical Engineering, Hanyang University, Ansan 15588, Republic of Korea*

Euichul Shin − *Department of Materials Science and Engineering, Korea Advanced Institute of Science and Technology (KAIST), Daejeon 34141, Republic of Korea*

Hionsuck Baik − *Korea Basic Science Institute (KBSI), Seoul 02841, Republic of Korea;* orcid.org/0000-0002-5745-4404

Jihan Kim − *Department of Chemical and Biomolecular Engineering, KAIST, Daejeon 34141, Republic of Korea;* orcid.org/0000-0002-3844-8789

Complete contact information is available at: https://pubs.acs.org/10.1021/acsnano.5c11229

Author Contributions

[¶]D.J., H.S. and J.-H.C. contributed equally to this work. H.S. and J.A. conceived the idea. D.J., H.S., and J.-H.C. designed and carried out all the experiments. I.-D.K. and S.-Y.C. supervised the project. H.K. and J.K. carried out modeling and simulation works. S.P. operated the IPL equipment. S.-H.C. assisted the electrochemical measurements. C.P., D.-H.K., and E.S. assisted with materials synthesis and discussion. H.B. carried out S/TEM measurements. All authors discussed the results and assisted during manuscript preparation.

Notes

The authors declare no competing financial interest.

ACKNOWLEDGMENTS

This work was also supported by Semiconductor-Secondary Battery Interfacing Platform Technology Development Project of NNFC in 2025. This work was supported by the National Research Foundation of Korea (NRF) grant funded by the Korea government (MSIT) (No. RS-2024-00435493). This work was supported by the National Research Foundation of Korea (NRF) grant funded by the Korea government (MSIT) (No. RS-2023-00236572).

REFERENCES

(1) Titirici, M.-M.; White, R. J.; Brun, N.; Budarin, V. L.; Su, D. S.; del Monte, F.; Clark, J. H.; MacLachlan, M. J. Sustainable Carbon Materials. *Chem. Soc. Rev.* **2015**, *44*, 250−290.

(2) Anjos, D. M.; McDonough, J. K.; Perre, E.; Brown, G. M.; Overbury, S. H.; Gogotsi, Y.; Presser, V. Pseudocapacitance and Performance Stability of Quinone-Coated Carbon Onions. *Nano Energy* **2013**, *2*, 702−712.

(3) Pech, D.; Brunet, M.; Durou, H.; Huang, P.; Mochalin, V.; Gogotsi, Y.; Taberna, P.-L.; Simon, P. Ultrahigh-Power Micrometre-Sized Supercapacitors Based on Onion-Like Carbon. *Nat. Nanotechnol.* **2010**, *5*, 651−654.

(4) Camisasca, A.; Sacco, A.; Brescia, R.; Giordani, S. Boron/Nitrogen-Codoped Carbon Nano-Onion Electrocatalysts for the Oxygen Reduction Reaction. *ACS Appl. Nano Mater.* **2018**, *1*, 5763−5773.

(5) Goclon, J.; Bankiewicz, B.; Kolek, P.; Winkler, K. Role of Nitrogen Doping in Stoichiometric and Defective Carbon Nano-Onions: Structural Diversity from DFT Calculations. *Carbon* **2021**, *176*, 198−208.

(6) Mohapatra, D.; Dhakal, G.; Sayed, M. S.; Subramanya, B.; Shim, J.-J.; Parida, S. Sulfur Doping: Unique Strategy to Improve the Supercapacitive Performance of Carbon Nano-Onions. *ACS Appl. Mater. Interfaces* **2019**, *11*, 8040−8050.

(7) Du, J.; Chen, J.; Zhang, C.; Jiang, G. Screening Out the Transition Metal Single Atom Supported on Onion-Like Carbon (OLC) for the Hydrogen Evolution Reaction. *Inorg. Chem.* **2023**, *62*, 1001−1006.

(8) Liu, D.; Li, X.; Chen, S.; Yan, H.; Wang, C.; Wu, C.; Haleem, Y. A.; Duan, S.; Lu, J.; Ge, B.; Ajayan, P. M.; Luo, Y.; Jiang, J.; Song, L. Atomically Dispersed Platinum Supported on Curved Carbon Supports for Efficient Electrocatalytic Hydrogen Evolution. *Nat. Energy* **2019**, *4*, 512−518.

(9) Yan, X.; Duan, P.; Zhang, F.; Li, H.; Zhang, H.; Zhao, M.; Zhang, X.; Xu, B.; Pennycook, S. J.; Guo, J. Stable Single-Atom Platinum Catalyst Trapped in Carbon Onion Graphitic Shells for

Improved Chemoselective Hydrogenation of Nitroarenes. *Carbon* **2019**, *143*, 378−384.
(10) Simon, P.; Gogotsi, Y. Materials for Electrochemical Capacitors. *Nat. Mater.* **2008**, *7*, 845−854.
(11) Zhang, C.; Du, H.; Ma, K.; Yuan, Z. Ultrahigh-Rate Supercapacitor Based on Carbon Nano-Onion/Graphene Hybrid Structure Toward Compact Alternating Current Filter. *Adv. Energy Mater.* **2020**, *10*, 2002132.
(12) Zhang, C.; Li, J.; Liu, E.; He, C.; Shi, C.; Du, X.; Hauge, R. H.; Zhao, N. Synthesis of Hollow Carbon Nano-Onions and Their Use for Electrochemical Hydrogen Storage. *Carbon* **2012**, *50*, 3513−3521.
(13) Sharma, A.; Agrawal, A.; Pandey, G.; Kumar, S.; Awasthi, K.; Awasthi, A. Carbon Nano-Onion-Decorated ZnO Composite-Based Enzyme-Less Electrochemical Biosensing Approach for Glucose. *ACS Omega* **2022**, *7*, 37748−37756.
(14) Yang, J.; Zhang, Y.; Kim, D. Y. Electrochemical Sensing Performance of Nanodiamond-Derived Carbon Nano-Onions: Comparison with Multiwalled Carbon Nanotubes, Graphite Nanoflakes, and Glassy Carbon. *Carbon* **2016**, *98*, 74−82.
(15) Xu, S.; Wang, M.; Saranya, G.; Chen, N.; Zhang, L.; He, Y.; Wu, L.; Gong, Y.; Yao, Z.; Wang, G.; Wang, Z.; Zhao, S.; Tang, H.; Chen, M.; Gou, H. Pressure-Driven Catalyst Synthesis of Co-Doped Fe_3C@Carbon Nano-Onions for Efficient Oxygen Evolution Reaction. *Appl. Catal., B* **2020**, *268*, 118385.
(16) Cebik, J.; McDonough, J. K.; Peerally, F.; Medrano, R.; Neitzel, I.; Gogotsi, Y.; Osswald, S. Raman Spectroscopy Study of the Nanodiamond-to-Carbon Onion Transformation. *Nanotechnology* **2013**, *24*, 205703.
(17) Portet, C.; Yushin, G.; Gogotsi, Y. Electrochemical Performance of Carbon Onions, Nanodiamonds, Carbon Black and Multiwalled Nanotubes in Electrical Double Layer Capacitors. *Carbon* **2007**, *45*, 2511−2518.
(18) Chen, L. C.; Wen, C. Y.; Liang, C. H.; Hong, W. K.; Chen, K. J.; Cheng, H. C.; Shen, C. S.; Wu, C. T.; Chen, K. H. Controlling Steps during Early Stages of the Aligned Growth of Carbon Nanotubes Using Microwave Plasma Enhanced Chemical Vapor Deposition. *Adv. Funct. Mater.* **2002**, *12*, 687−692.
(19) Chen, X. H.; Deng, F. M.; Wang, J. X.; Yang, H. S.; Wu, G. T.; Zhang, X. B.; Peng, J. C.; Li, W. Z. New Method of Carbon Onion Growth by Radio-Frequency Plasma-Enhanced Chemical Vapor Deposition. *Chem. Phys. Lett.* **2001**, *336*, 201−204.
(20) Manawi, Y. M.; Ihsanullah; Samara, A.; Al-Ansari, T.; Atieh, M. A. A Review of Carbon Nanomaterials' Synthesis via the Chemical Vapor Deposition (CVD) Method. *Materials* **2018**, *11*, 822.
(21) Sano, N.; Wang, H.; Alexandrou, I.; Chhowalla, M.; Teo, K. B. K.; Amaratunga, G. A. J.; et al. Properties of Carbon Onions Produced by an Arc Discharge in Water. *J. Appl. Phys.* **2002**, *92*, 2783−2788.
(22) Sano, N.; Wang, H.; Chhowalla, M.; Alexandrou, I.; Amaratunga, G. A. J. Synthesis of Carbon "Onions" in Water. *Nature* **2001**, *414*, 506−507.
(23) Tripathi, K. M.; Bhati, A.; Singh, A.; Gupta, N. R.; Verma, S.; Sarkar, S.; Sonkar, S. K. From the Traditional Way of Pyrolysis to Tunable Photoluminescent Water Soluble Carbon Nano-Onions for Cell Imaging and Selective Sensing of Glucose. *RSC Adv.* **2016**, *6*, 37319−37329.
(24) Xin, Y.; Odachi, K.; Shirai, T. Fabrication of Ultra-Bright Carbon Nano-Onions via a One-Step Microwave Pyrolysis of Fish Scale Waste in Seconds. *Green Chem.* **2022**, *24*, 3969−3976.
(25) Gorelik, T.; Urban, S.; Falk, F.; Kaiser, U.; Glatzel, U. Carbon Onions Produced by Laser Irradiation of Amorphous Silicon Carbide. *Chem. Phys. Lett.* **2003**, *373*, 642−645.
(26) Hu, S.; Bai, P.; Tian, F.; Cao, S.; Sun, J. Hydrophilic Carbon Onions Synthesized by Millisecond Pulsed Laser Irradiation. *Carbon* **2009**, *47*, 876−883.
(27) Cui, X.; Ruan, Q.; Zhuo, X.; Xia, X.; Hu, J.; Fu, R.; Li, Y.; Wang, J.; Xu, H. Photothermal Nanomaterials: A Powerful Light-to-Heat Converter. *Chem. Rev.* **2023**, *123*, 6891−6952.
(28) Yi, X.; Duan, Q.-Y.; Wu, F.-G. Low-Temperature Photothermal Therapy: Strategies and Applications. *Research* **2021**, *2021*, 9816594.
(29) Ren, Y.; Yan, Y.; Qi, H. Photothermal Conversion and Transfer in Photothermal Therapy: From Macroscale to Nanoscale. *Adv. Colloid Interface Sci.* **2022**, *308*, 102753.
(30) Cha, J.-H.; Kim, D.-H.; Park, C.; Choi, S.-J.; Jang, J.-S.; Yang, S. Y.; Kim, I. D.; Choi, S. Y. Low-Thermal-Budget Doping of 2D Materials in Ambient Air Exemplified by Synthesis of Boron-Doped Reduced Graphene Oxide. *Adv. Sci.* **2020**, *7*, 1903318.
(31) Kim, D.-H.; Cha, J.-H.; Shim, G.; Kim, Y. H.; Jang, J.-S.; Shin, H.; Ahn, J.; Choi, S. Y.; Kim, I. D. Flash-Thermochemical Engineering of Phase and Surface Activity on Metal Oxides. *Chem.* **2022**, *8*, 1014−1033.
(32) Shin, E.; Kim, D.-H.; Cha, J.-H.; Yun, S.; Shin, H.; Ahn, J.; Jang, J.-S.; Baek, J. W.; Park, C.; Ko, J.; Park, S.; Choi, S.-Y.; Kim, I. D. Ultrafast Ambient-Air Exsolution on Metal Oxide via Momentary Photothermal Effect. *ACS Nano* **2022**, *16*, 18133−18142.
(33) Beck, R. A.; Huang, Y.; Petrone, A.; Abbott, J. W.; Pauzauskie, P. J.; Li, X. Electronic Structures and Spectroscopic Signatures of Noble-Gas-Doped Nanodiamonds. *ACS Phys. Chem. Au* **2023**, *3*, 299−310.
(34) Han, P.; Antonov, D.; Wrachtrup, J.; Bester, G. Surface-Bound States in Nanodiamonds. *Phys. Rev. B* **2017**, *95*, 195428.
(35) Cho, D.; Suh, J. M.; Nam, S. H.; Park, S. Y.; Park, M.; Lee, T. H.; Choi, K. S.; Lee, J.; Ahn, C.; Jang, H. W.; Shim, Y.-S.; Jeon, S. Optically Activated 3D Thin-Shell TiO_2 for Super-Sensitive Chemoresistive Responses: Toward Visible Light Activation. *Adv. Sci.* **2021**, *8*, 2001883.
(36) Xia, C.; Qiu, Y.; Xia, Y.; Zhu, P.; King, G.; Zhang, X.; Wu, Z.; Kim, J. Y.; Cullen, D. A.; Zheng, D.; Li, P.; Shakouri, M.; Heredia, E.; Cui, P.; Alshareef, H. N.; Hu, Y.; et al. General Synthesis of Single-Atom Catalysts with High Metal Loading Using Graphene Quantum Dots. *Nat. Chem.* **2021**, *13*, 887−894.
(37) Li, Z.; Chen, Y.; Ji, S.; Tang, Y.; Chen, W.; Li, A.; Zhao, J.; Xiong, Y.; Wu, Y.; Gong, Y.; Yao, T.; Liu, W.; Zheng, L.; Dong, J.; Wang, Y.; Zhuang, Z.; Xing, W.; He, C.-T.; Peng, C.; et al. Iridium Single-Atom Catalyst on Nitrogen-Doped Carbon for Formic Acid Oxidation Synthesized Using a General Host−Guest Strategy. *Nat. Chem.* **2020**, *12*, 764−772.
(38) Zheng, X.; Gao, X.; Vilá, R. A.; Jiang, Y.; Wang, J.; Xu, R.; Zhang, R.; Xiao, X.; Zhang, P.; Greenburg, L. C.; Yang, Y.; Xin, H. L.; Zheng, X.; Cui, Y. Hydrogen-Substituted Graphdiyne-Assisted Ultrafast Sparking Synthesis of Metastable Nanomaterials. *Nat. Nanotechnol.* **2023**, *18*, 153−159.
(39) Yao, Y.; Huang, Z.; Xie, P.; Wu, L.; Ma, L.; Li, T.; Pang, Z.; Jiao, M.; Liang, Z.; Gao, J.; He, Y.; Kline, D. J.; Zachariah, M. R.; Wang, C.; Lu, J.; Wu, T.; Li, T.; Wang, C.; Shahbazian-Yassar, R.; Hu, L. High Temperature Shockwave Stabilized Single Atoms. *Nat. Nanotechnol.* **2019**, *14*, 851−857.
(40) Yao, Y.; Huang, Z.; Xie, P.; Lacey, S. D.; Jacob, R. J.; Xie, H.; Chen, F.; Nie, A.; Pu, T.; Rehwoldt, M.; Yu, D.; Zachariah, M. R.; Wang, C.; Shahbazian-Yassar, R.; Li, J.; Hu, L. Carbothermal Shock Synthesis of High-Entropy-Alloy Nanoparticles. *Science* **2018**, *359*, 1489−1494.
(41) Kim, D.-H.; Cha, J.-H.; Chong, S.; Cho, S.-H.; Shin, H.; Ahn, J.; Jeon, D.; Kim, J.; Choi, S.-Y.; Kim, I. D. Flash-Thermal Shock Synthesis of Single Atoms in Ambient Air. *ACS Nano* **2023**, *17*, 23347−23358.
(42) Cha, J.-H.; Cho, S.-H.; Kim, D.-H.; Jeon, D.; Park, S.; Jung, J. W.; Kim, I. D.; Choi, S.-Y. Flash-Thermal Shock Synthesis of High-Entropy Alloys toward High-Performance Water Splitting. *Adv. Mater.* **2023**, *35*, 2305222.
(43) Qiao, B.; Wang, A.; Yang, X.; Allard, L. F.; Jiang, Z.; Cui, Y.; Liu, J.; Li, J.; Zhang, T. Single-Atom Catalysis of CO Oxidation Using Pt_1/FeOx. *Nat. Chem.* **2011**, *3*, 634−641.
(44) Marcinkowski, M. D.; Darby, M. T.; Liu, J.; Wimble, J. M.; Lucci, F. R.; Lee, S.; Michaelides, A.; Flytzani-Stephanopoulos, M.; Stamatakis, M.; Sykes, E. C. H. Pt/Cu Single-Atom Alloys as Coke-Resistant Catalysts for Efficient C−H Activation. *Nat. Chem.* **2018**, *10*, 325−332.

https://doi.org/10.1021/acsnano.5c11229
ACS Nano XXXX, XXX, XXX−XXX

(45) Cheng, N.; Stambula, S.; Wang, D.; Banis, M. N.; Liu, J.; Riese, A.; Xiao, B.; Li, R.; Sham, T.-K.; Liu, L.-M.; Botton, G. A.; Sun, X. Platinum Single-Atom and Cluster Catalysis of the Hydrogen Evolution Reaction. *Nat. Commun.* **2016**, *7*, 13638.
(46) Lee, B.-H.; Park, S.; Kim, M.; Sinha, A. K.; Lee, S. C.; Jung, E.; Chang, W. J.; Lee, K.-S.; Kim, J. H.; Cho, S.-P.; Kim, H.; Nam, K. T.; Hyeon, T. Reversible and Cooperative Photoactivation of Single-Atom Cu/TiO_2 Photocatalysts. *Nat. Mater.* **2019**, *18*, 620−626.
(47) Hannagan, R. T.; Giannakakis, G.; Réocreux, R.; Schumann, J.; Finzel, J.; Wang, Y.; Michaelides, A.; Deshlahra, P.; Christopher, P.; Flytzani-Stephanopoulos, M.; Stamatakis, M.; Sykes, E. C. H. First-Principles Design of a Single-Atom−Alloy Propane Dehydrogenation Catalyst. *Science* **2021**, *372*, 1444−1447.
(48) Shin, H.; Ko, J.; Park, C.; Kim, D.-H.; Ahn, J.; Jang, J.-S.; Kim, Y. H.; Cho, S.-H.; Baik, H.; Kim, I. D. Sacrificial Template-Assisted Synthesis of Inorganic Nanosheets with High-Loading Single-Atom Catalysts: A General Approach. *Adv. Funct. Mater.* **2022**, *32*, 2110485.
(49) Kamat, G. A.; Zamora Zeledón, J. A.; Gunasooriya, G. T. K. K.; Dull, S. M.; Perryman, J. T.; Nørskov, J. K.; Stevens, M. B.; Jaramillo, T. F. Acid Anion Electrolyte Effects on Platinum for Oxygen and Hydrogen Electrocatalysis. *Commun. Chem.* **2022**, *5*, 20.
(50) Xu, S.; Wang, M.; Saranya, G.; Chen, N.; Zhang, L.; He, L.; Wu, L.; Gong, Y.; Yao, Z.; Wang, G.; Wang, Z.; Zhao, S.; Tang, H.; Chen, M.; Gou, H. Pressure-Driven Catalyst Synthesis of Co-Doped Fe_3C@Carbon Nano-Onions for Efficient Oxygen Evolution Reaction. *Appl. Catal., B* **2020**, *268*, 118385.
(51) Tang, H.; Yuan, X.; Yu, P.; Hu, Q.; Wang, M.; Yao, Y.; Wu, L.; Zou, Q.; Ke, Y.; Zhao, Y.; Wang, L.; Li, X.; Yang, W.; Gou, H.; Mao, H.-K.; Mao, W. L. Revealing the Formation Mechanism of Ultrahard Nanotwinned Diamond from Onion Carbon. *Carbon* **2018**, *129*, 159−167.
(52) Kuznetsov, V. L.; Chuvilin, A. L.; Butenko, Y. V.; Mal'kov, I. Y.; Titov, V. M. Onion-Like Carbon from Ultra-Disperse Diamond. *Chem. Phys. Lett.* **1994**, *222*, 343−348.
(53) Jain, A.; Ong, S. P.; Hautier, G.; Chen, W.; Richards, W. D.; Dacek, S.; Cholia, S.; Gunter, D.; Skinner, D.; Ceder, G.; Persson, K. A. Commentary: The Materials Project: A Materials Genome Approach to Accelerating Materials Innovation. *APL Mater.* **2013**, *1*, 011002.
(54) Bródka, A.; Hawełek, Ł.; Burian, A.; Tomita, S.; Honkimäki, V. Molecular Dynamics Study of Structure and Graphitization Process of Nanodiamonds. *J. Mol. Struct.* **2008**, *887*, 34−40.
(55) Tran, R.; Xu, Z.; Radhakrishnan, B.; Winston, D.; Sun, W.; Persson, K. A.; Ong, S. P. Surface Energies of Elemental Crystals. *Sci. Data* **2016**, *3*, 160080.
(56) Aktulga, H. M.; Fogarty, J. C.; Pandit, S. A.; Grama, A. Y. Parallel Reactive Molecular Dynamics: Numerical Methods and Algorithmic Techniques. *Parallel Comput.* **2012**, *38*, 245−259.
(57) Thompson, A. P.; Aktulga, H. M.; Berger, R.; Bolintineanu, D. S.; Brown, W. M.; Crozier, P. S.; in't Veld, P. J.; Kohlmeyer, A.; Moore, S. G.; Nguyen, T. D.; Shan, R.; Stevens, M. J.; Tranchida, J.; Trott, C.; Plimpton, S. J. LAMMPS—A Flexible Simulation Tool for Particle-Based Materials Modeling at the Atomic, Meso, and Continuum Scales. *Comput. Phys. Commun.* **2022**, *271*, 108171.
(58) Chenoweth, K.; van Duin, A. C. T.; Goddard, W. A. ReaxFF Reactive Force Field for Molecular Dynamics Simulations of Hydrocarbon Oxidation. *J. Phys. Chem. A* **2008**, *112*, 1040−1053.
(59) Sanz-Navarro, C. F.; Åstrand, P.-O.; Chen, D.; Rønning, M.; van Duin, A. C. T.; Jacob, T.; Goddard, W. A. Molecular Dynamics Simulations of the Interactions between Platinum Clusters and Carbon Platelets. *J. Phys. Chem. A* **2008**, *112*, 1392−1402.
(60) Stukowski, A. Visualization and Analysis of Atomistic Simulation Data with OVITO—The Open Visualization Tool. *Modell. Simul. Mater. Sci. Eng.* **2010**, *18*, 015012.

https://doi.org/10.1021/acsnano.5c11229
ACS Nano XXXX, XXX, XXX−XXX